



# High accuracy transfer printing of single-mode membrane silicon photonic devices

JOHN MCPHILLIMY,<sup>1,\*</sup> BENOIT GUILHABERT,<sup>1</sup> CHARALAMBOS KLITIS,<sup>2</sup> MARTIN D. DAWSON,<sup>1</sup> MARC SOREL,<sup>2</sup> AND MICHAEL J. STRAIN<sup>1</sup>

<sup>1</sup>*Institute of Photonics, Dept. of Physics, University of Strathclyde, Glasgow G1 1RD, UK*

<sup>2</sup>*School of Engineering, University of Glasgow, Glasgow, Oakfield Avenue, Glasgow, G12 8LT, UK*

\**john.mcphillimy@strath.ac.uk*

**Abstract:** A transfer printing (TP) method is presented for the micro-assembly of integrated photonic devices from suspended membrane components. Ultra thin membranes with thickness of 150nm are directly printed without the use of mechanical support and adhesion layers. By using a correlation alignment scheme vertical integration of single-mode silicon waveguides is achieved with an average placement accuracy of  $100\pm 70$ nm. Silicon (Si)  $\mu$ -ring resonators are also fabricated and show controllable optical coupling by varying the lateral absolute position to an underlying Si bus waveguide.

Published by The Optical Society under the terms of the [Creative Commons Attribution 4.0 License](#). Further distribution of this work must maintain attribution to the author(s) and the published article's title, journal citation, and DOI.

**OCIS codes:** (250.5300) Photonic integrated circuits; (130.0130) Integrated optics; (230.0230) Optical devices.

## References and links

1. J. Doylend and A. Knights, "The evolution of silicon photonics as an enabling technology for optical interconnection," *Laser & Photonics Rev.* **6**, 504–525 (2012).
2. D. Liang, X. Huang, G. Kurczveil, M. Fiorentino, and R. G. Beausoleil, "Integrated finely tunable microring laser on silicon," *Nat. Photonics* **10**, 719–722 (2016).
3. M. J. R. Heck, J. F. Bauters, M. L. Davenport, J. K. Doylend, S. Jain, G. Kurczveil, S. Srinivasan, and J. E. Bowers, "Hybrid Silicon Photonic Integrated Circuit Technology," *IEEE J. Sel. Top. Quantum Electron.* **19**, 6100117–6100117 (2013).
4. G. Roelkens, A. Abassi, P. Cardile, U. Dave, A. de Groote, Y. de Koninck, S. Dhoore, X. Fu, A. Gassenq, N. Hattasan, Q. Huang, S. Kumari, S. Keyvaninia, B. Kuyken, L. Li, P. Mechet, M. Muneeb, D. Sanchez, H. Shao, T. Spuesens, A. Subramanian, S. Uvin, M. Tassaert, K. van Gasse, J. Verbist, R. Wang, Z. Wang, J. Zhang, J. van Campenhout, X. Yin, J. Bauwelinck, G. Morthier, R. Baets, and D. van Thourhout, "III-V-on-Silicon Photonic Devices for Optical Communication and Sensing," *Photonics* **2**, 969–1004 (2015).
5. N. Volet, A. Spott, E. J. Stanton, M. L. Davenport, L. Chang, J. D. Peters, T. C. Briles, I. Vurgaftman, J. R. Meyer, and J. E. Bowers, "Semiconductor optical amplifiers at 2.0- $\mu$ m wavelength on silicon," *Laser & Photonics Rev.* **11**, 1600165 (2017).
6. K. Chen, Q. Huang, J. Zhang, J. Cheng, X. Fu, C. Zhang, K. Ma, Y. Shi, D. V. Thourhout, G. Roelkens, L. Liu, and S. He, "Wavelength-multiplexed duplex transceiver based on III-v/si hybrid integration for off-chip and on-chip optical interconnects," *IEEE Photonics J.* **8**, 1–10 (2016).
7. R. Wang, A. Vasiliev, M. Muneeb, A. Malik, S. Sprengel, G. Boehm, M.-C. Amann, I. Šimonytė, A. Vizbaras, K. Vizbaras, R. Baets, and G. Roelkens, "III-V-on-Silicon Photonic Integrated Circuits for Spectroscopic Sensing in the 2–4  $\mu$ m Wavelength Range," *Sensors* **17**, 1788 (2017).
8. S. Lin, X. Zheng, J. Yao, S. S. Djordjevic, J. E. Cunningham, J.-H. Lee, I. Shubin, Y. Luo, J. Bovington, D. Y. Lee, H. D. Thacker, K. Raj, and A. V. Krishnamoorthy, "Efficient, tunable flip-chip-integrated III-V/Si hybrid external-cavity laser array," *Opt. Express* **24**, 21454 (2016).
9. T. Ahmed, A. A. Khan, G. Vigil, J. M. Kulick, G. H. Bernstein, A. J. Hoffman, and S. S. Howard, "Optical quilt packaging: A new chip-to-chip optical coupling and alignment process for modular sensors," in "CLEO: 2014," (OSA, 2014).
10. T. Ahmed, T. Lu, T. Butler, J. Kulick, G. Bernstein, A. Hoffman, D. Hall, and S. Howard, "Mid-Infrared Waveguide Array Inter-chip Coupling using Optical Quilt Packaging," *IEEE Photonics Technol. Lett.* **1135**, 1–1 (2017).
11. G. Roelkens, L. Liu, D. Liang, R. Jones, A. Fang, B. Koch, and J. Bowers, "III-V/silicon photonics for on-chip and intra-chip optical interconnects," *Laser Photonics Rev.* **4**, 751–779 (2010).
12. G. Crosnier, D. Sanchez, S. Bouchoule, P. Monnier, G. Beaudoin, I. Sagnes, R. Raj, and F. Raineri, "Hybrid indium phosphide-on-silicon nanolaser diode," *Nat. Photonics* **11**, 297–300 (2017).

13. M. A. Meitl, Z.-T. Zhu, V. Kumar, K. J. Lee, X. Feng, Y. Y. Huang, I. Adesida, R. G. Nuzzo, and J. A. Rogers, "Transfer printing by kinetic control of adhesion to an elastomeric stamp," *Nat. Mater.* **5**, 33–38 (2006).
14. C. A. Bower, E. Menard, and P. E. Garrou, "Transfer printing: An approach for massively parallel assembly of microscale devices," in "2008 58th Electronic Components and Technology Conference," (IEEE, 2008).
15. A. De Groot, P. Cardile, A. Z. Subramanian, A. M. Fecioru, C. Bower, D. Delbeke, R. Baets, and G. Roelkens, "Transfer-printing-based integration of single-mode waveguide-coupled III-V-on-silicon broadband light emitters," *Opt. Express* **24**, 13754 (2016).
16. J. Zhang, A. D. Groot, A. Abbasi, R. Loi, J. O'Callaghan, B. Corbett, A. J. Trindade, C. A. Bower, and G. Roelkens, "Silicon photonics fiber-to-the-home transceiver array based on transfer-printing-based integration of III-V photodetectors," *Opt. Express* **25**, 14290 (2017).
17. A. J. Trindade, B. Guilhabert, E. Y. Xie, R. Ferreira, J. J. D. McKendry, D. Zhu, N. Laurand, E. Gu, D. J. Wallis, I. M. Watson, C. J. Humphreys, and M. D. Dawson, "Heterogeneous integration of gallium nitride light-emitting diodes on diamond and silica by transfer printing," *Opt. Express* **23**, 9329–9338 (2015).
18. C. Prevatte, E. Radauscher, M. A. Meitl, D. Gomez, K. Ghosal, S. Bonafede, B. Raymond, T. Moore, A. J. Trindade, P. Hines, and C. A. Bower, "Miniature Heterogeneous Fan-Out Packages for High-Performance, Large-Format Systems," *IEEE* **5**, A23–A29 (2017).
19. D. Jevtics, A. Hurtado, B. Guilhabert, J. McPhillimy, G. Cantarella, Q. Gao, H. H. Tan, C. Jagadish, M. J. Strain, and M. D. Dawson, "Integration of semiconductor nanowire lasers with polymeric waveguide devices on a mechanically flexible substrate," *Nano Lett.* **17**, 5990–5994 (2017).
20. N. Ye, G. Muliuk, J. Zhang, A. Abbasi, A. J. Trindade, C. Bower, D. V. Thourhout, and G. Roelkens, "Transfer print integration of waveguide-coupled germanium photodiodes onto passive silicon photonic ICs," *J. Light. Technol.* **36**, 1249–1254 (2018).
21. J. Yoon, S. M. Lee, D. Kang, M. A. Meitl, C. A. Bower, and J. A. Rogers, "Heterogeneously Integrated Optoelectronic Devices Enabled by Micro-Transfer Printing," *Adv. Opt. Mater.* **3**, 1313–1335 (2015).
22. N. Ye, G. Muliuk, A. J. Trindade, C. Bower, J. Zhang, S. Uvin, D. V. Thourhout, and G. Roelkens, "High-alignment-accuracy transfer printing of passive silicon waveguide structures," *Opt. Express* **26**, 2023 (2018).
23. M. Gnan, S. Thoms, D. Macintyre, R. De La Rue, and M. Sorel, "Fabrication of low-loss photonic wires in silicon-on-insulator using hydrogen silsesquioxane electron-beam resist," *Electron. Lett.* **44**, 115 (2008).
24. J. Wu, S. Kim, W. Chen, A. Carlson, K.-C. Hwang, Y. Huang, and J. A. Rogers, "Mechanics of reversible adhesion," *Soft Matter* **7**, 8657 (2011).
25. C. Wang and T. Suga, "Moiré Method for Nanoprecision Wafer-to-Wafer Alignment : Theory , Simulation and Application," *Packag. Technol.* pp. 219–224 (2009).
26. S. Kawashima, M. Imada, K. Ishizaki, and S. Noda, "High-Precision Alignment and Bonding System for the Fabrication of 3-D Nanostructures," *J. Microelectromechanical Syst.* **16**, 1140–1144 (2007).
27. E. Anderson, "Sub-pixel alignment for direct-write electron beam lithography," *Microelectron. Eng.* **73-74**, 74–79 (2004).
28. A. Broers, A. Hoole, and J. Ryan, "Electron beam lithography—resolution limits," *Microelectron. Eng.* **32**, 131–142 (1996).
29. P. L. Stiles, "Direct deposition of micro- and nanoscale hydrogels using Dip Pen Nanolithography ( DPN )," *Nat. Method* **7**, i–ii (2010).
30. W. Bogaerts, P. de Heyn, T. van Vaerenbergh, K. de Vos, S. Kumar Selvaraja, T. Claes, P. Dumon, P. Bienstman, D. van Thourhout, and R. Baets, "Silicon microring resonators," *Laser Photonics Rev.* **6**, 47–73 (2012).

## 1. Introduction

The silicon-on-insulator (SOI) material platform is rapidly becoming the standard for realisation of large scale photonic integrated circuits. The high index contrast and CMOS fabrication compatibility enable high yield production of compact devices using established foundry processing, which offers a broad scope of photonic components [1].

Due to the challenge introduced in producing efficient light sources in silicon [2] there has been significant recent work in the integration of III-V materials on silicon [3]. Furthermore, the ability to vertically integrate waveguiding layers has the added potential benefit of allowing fabrication of 3D integrated circuits that will reduce the on-chip footprint and increase potential complexity with respect to 2D architectures. Progress in these areas will benefit applications from the next generation of optical communications and interconnects [4–6] to optical sensing [7].

The improved performance promised by such systems has accelerated the development of a range of techniques for the fabrication of efficient multi-layered hybrid photonic circuits. They include flip chip integration [8] and quilt packaging for chip-to-chip interconnecting [9]. Such techniques have an alignment accuracy restricted to several micrometres with efficient coupling

of back-end aligned structures limited to tens of micrometres in width [10]. One of the most well established methods for high accuracy 3D integration is wafer bonding [11, 12]. Unprocessed dies are bonded to a non-native substrate either by direct bonding or use of an adhesive bonding layer. After which, the integrated components are defined by further stages of lithography, reactive ion etching and metal deposition.

One potential alternative is transfer printing (TP). TP is an attractive approach for vertical device integration technologies, and unlike wafer bonding it provides an effective route for back-end processing, offering greater flexibility and opportunities regarding heterogeneous integration. First proposed by Rogers *et al* [13], transfer printing is a pick-and-place procedure in which an elastomeric stamp transfers selectively removed coupons of material from its host platform to a non-native substrate. The process promotes high yield, densely packed device printing. As such, TP can integrate pre-fabricated structures in a massively parallel and scalable fashion [14] with recent device demonstrations ranging from III-V-on Si active devices [15, 16], micro-LEDs [17, 18], and flexible integrated circuits [19]. Current TP systems have demonstrated an absolute alignment accuracy within  $\pm 1\mu\text{m}$  [20], therefore to achieve nanoscale device integration requires post bonding fabrication processing steps to lithographically align structures [21]; or the design of tapered couplers to decrease the necessary tolerances [22].

In this work, vertical integration of fully fabricated single-mode silicon membrane devices is presented. This method introduces a solution for high precision integration of single-mode optical waveguides without relying on back-end processing and allows the transfer of ultra-thin membranes (150nm thickness) without the need for intermediate processing of mechanical support layers. The accuracy of the alignment procedure is demonstrated by the controlled micro-assembly of vertically coupled Si ring resonator devices to underlying SOI bus waveguides. The optical performance of the resonators is defined through the absolute alignment of the devices giving control over the resonator coupling coefficient.

## 2. Fabrication and micro-transfer printing of Si membrane devices

### 2.1. Device fabrication

Both donor and receiver SOI wafers are comprised of a 220nm thick silicon core above a  $2\mu\text{m}$  buried oxide layer. The full fabrication process for the suspended ultra-thin Si membrane devices is shown in Fig. 1(a). The waveguide structures alongside a support frame - to increase membrane stiffness - are defined in a 240nm-thick ZEP resist layer using electron-beam lithography. The pattern is transferred to the Si layer by shallow etching (to a depth of 70nm) using an inductively coupled plasma (ICP) reactive ion etching process [23]. Following this, a PMMA layer is deposited on top of the Si which is subsequently patterned to define the surrounding  $10\mu\text{m}$  wide trench and accompanying anchor supports, with a full etch using ICP removing the surrounding Si.

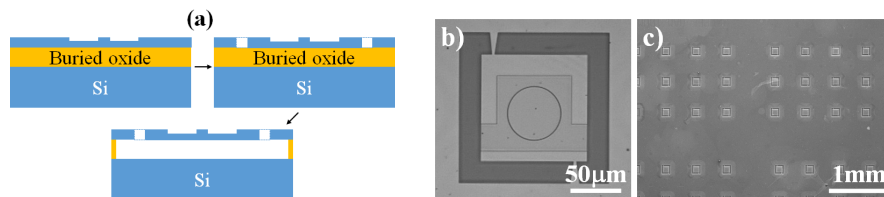


Fig. 1. (a) Schematic illustration of membrane device fabrication and suspension; (b) SEM image of a single suspended membrane containing a Si ring resonator; (c) SEM image of suspended patterned membrane arrays on a single SOI wafer.

The membrane suspension is achieved by removing the buried oxide layer using a vapour

hydrofluoric acid (VHF) etch leaving the membrane attached solely to the supporting anchors, which are tapered from  $9\mu\text{m}$  to  $3\mu\text{m}$  in contact with the membrane. A fully fabricated membrane containing a patterned Si ring resonator is shown in Fig. 1(b). Since the membrane devices will be used to populate PICs on a secondary substrate, they can be densely arrayed for fabrication as shown in Fig. 1(c).

For future 3D integration of multiple membranes an inter-membrane optical spacer layer may be implemented to allow controllable vertical coupling and avoid the accumulation of thick silicon layers. This can be achieved by applying an HF resistant polymer or dielectric cladding layer prior to the membrane device suspension and removal from the donor substrate. Furthermore, the cumulative curvature of the printed membranes could result in possible mechanical issues over multiple stacked layers. Future fabrication schemes could include planarized upper cladding layers to maintain parallelism between stacked membranes.

## 2.2. Transfer printing of Si membrane devices

Transfer printing was realized using a commercial dip-pen nano-patterning system (NanoInk Inc. NLP2000) that has been modified to incorporate a fixed stamp holder and for which custom control software has been developed. The process uses an elastomeric stamp's reversible adhesion properties to pick-up and place devices from a donor to a receiver substrate in a highly controllable method [24] as illustrated in Fig. 2(a). The elastomeric stamp is placed into contact with the membrane until fully in contact with the surface, with a quick retraction breaking the support anchors removing the device from the donor wafer. The membrane underside is then placed into contact with the receiver substrate. As the stamp is slowly released from the surface, the bonding force between the receiver and membrane overcomes the adhesion to the elastomeric stamp causing the membrane to release itself from the stamp and attach to the receiving substrate. The devices fabricated in this work were printed with the Si membrane underside in direct contact with the receiver Si and  $\text{SiO}_2$  BOX layers, without use of an intermediate adhesion layer such as divinylsiloxane-benzocyclobutene (DVS-BCB) or polymer as previously demonstrated [20].

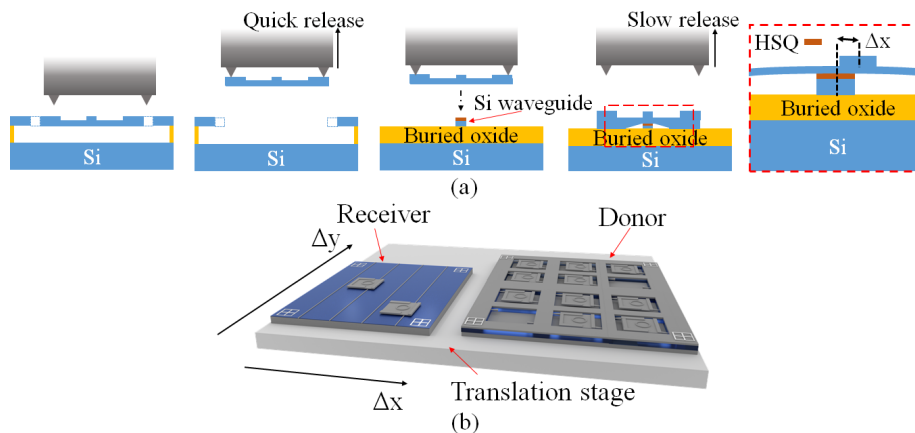


Fig. 2. (a) Schematic of transfer printing process of membrane devices from donor to receiver substrate, including magnified illustration of stacked device showing controlled lateral alignment of waveguide layers ( $\Delta x$ ) controlling coupling between waveguides. The HSQ intermediate layer thickness is  $\approx 100\text{nm}$ ; (b) Illustration of the micro-assembly of devices between two substrates positioned on the system's translation stage.

### 3. Accurate absolute alignment

The conventional approach for micro-assembly techniques employs optical overlay alignment which uses visual edge detection in extracting positional information from alignment markers. Small variations in the marker structure and resolution of the optical microscopy system limits possible absolute alignment to the micrometre scale.

There are a number of techniques that have been developed for optical and electron-beam lithography that can improve on this alignment. For example, laser Moire fringe alignment [25], infra-red transmission microscopy [26], and pattern correlation techniques [27].

In this work we used a pattern correlation scheme, imaged using the standard microscope optics of the transfer print tool with a feature size of below  $1\mu\text{m}$ . Fig. 2(b) shows a schematic of two substrates securely positioned on a translation stage. The placement of both donor and receiver substrates are carried out by hand with the initial sample positioning being judged by the user using the stage boundaries as a rough alignment reference. The initial x-y placement accuracy of the samples is in the mm range, with rotational accuracy in the mrad range. The linear translation stages within the modified NanoInk NLP2000 system are commercial (Nanomotion Ltd. HR4) motor driven actuators, achieving a specified encoder resolution of 5nm and a stage repeatability for both the x- and y-axis of  $\pm 25\text{nm}$ . Markers are fabricated on the samples in the same step as the first waveguide lithography layer, ensuring nanoscale alignment accuracy between the markers and waveguide structures on the corresponding donor and receiver samples [28].

The micro-assembly of single-mode Si waveguides with width  $\approx 500\text{nm}$  requires both high accuracy positional registration of devices on different substrates and a robust transfer mechanism. The printing process must maintain the absolute position of the membrane during printing, i.e. avoiding relative movement of the stamp, slippage or rotation during the bonding steps.

The alignment capabilities of the correlation technique were characterised using two complementary methods. First, the accuracy of detecting a pre-defined position is assessed by aligning two identical markers with a known separation on a single sample within our TP system. The comparison of multiple positional offset measurements calculates the error in our alignment procedure, using the TP system's translation stage. Second, the accuracy of depositing two physical structures on a single sample by a target separation is assessed. The structures are created by physically marking lines into a photoresist layer using a micro-tip array with each structure's position determined by using the correlation alignment procedure. The positional accuracy is measured using standard AFM technology. Error in the separation is a measure of the system absolute alignment accuracy.

#### *Measurement 1:*

A single silicon sample was fabricated by e-beam lithography with alignment markers spaced by 2mm with an accuracy of  $\pm 2\text{nm}$ , illustrated in Fig. 3(a).

The alignment procedure calculates the positional error between each marker as they are moved to the centre point of the TP system's field-of-view by the known 2mm separation. Both x and y correlation versus displacement curves for a single marker are shown in Fig. 3(b), with the marker correlation amplitude calculated as a function of local translation around the marker. As the correlation curve is symmetric, linear fitting both sides separately calculates an intersection point which determines the maximum point of correlation. This provides a maximum correlation intensity ( $\Delta x$ ,  $\Delta y$ ) corresponding to the marker's centre point relative to the translation stage coordinate system. The calculated positional offsets shown in Fig. 3(b) include the effects of the relative rotation of the sample to the stage translation grid and the errors of the alignment process. If the sample has some rotation with respect to the translation stage axes, then the 2mm marker-marker distance does not lie only on one axis and therefore offsets in both axes will be measured. Once these offsets have been accounted for, any residual deviation from the expected 2mm separation is due to errors in the marker alignment process. This procedure is repeated

between each marker giving the  $(x, y)$  positional errors for each correlation measurement, which enables the separation of the correlation technique alignment accuracy and the rotational offset. The measured marker separation can then be compared with the fabrication-defined value, giving alignment errors in both  $x$  and  $y$  directions as shown in table 1 for multiple repetitions of the procedure.

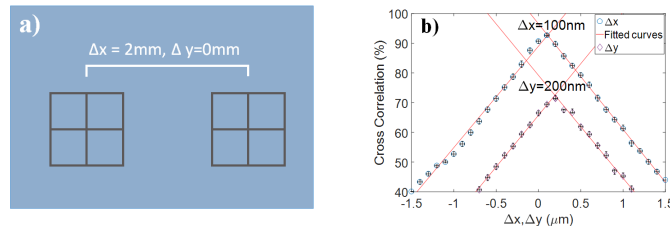


Fig. 3. (a) Schematic illustration of sample containing two identical registration markers with a known separation of 2mm (not to scale); (b) Plot shows the marker correlation amplitude as a function of local translation around the marker in both  $x$  and  $y$ . The positional offset values noted include both measurement errors and lateral offsets caused by relative rotation of the sample to the stage axes.

Table 1. Alignment error calculations

Meas.	Error: x-axis (nm)	Error: y-axis (nm)
1	90	10
2	10	70
3	80	10
4	90	67
5	11	70
Average error $\pm$ Std dev	$56 \pm 37.5$	$45 \pm 29$

An alignment accuracy of  $56 \pm 37.5$  nm for the  $x$ -axis and  $45 \pm 29$  nm for the  $y$ -axis over multiple measurements is achieved (table 1).

### Measurement 2:

Silicon nitride probe tip arrays deposit controlled amounts of materials onto surfaces in dip pen nanolithography processing [29]. Modifying the TP system by replacing the elastomeric stamp with the probe tips allows the production of physical indentation lines into a sample with the same positional accuracy as the TP pick-and-place procedure, as shown in Fig. 4. Alignment markers are patterned using direct-write laser lithography using a positive photoresist, and by using the correlation alignment technique implemented alongside the TP system the relatively aligned features are physically marked into the resist layer. The placement accuracy is measured by using AFM technology.

Using the correlation procedure, the absolute position of the fabricated alignment marker is calculated. A physical line is formed at a relative separation from the absolute marker position using the probe tips. This procedure is repeated producing a second indent line with a target separation of  $5 \mu\text{m}$  between each indentation. Fig. 4(b) shows a 3D AFM measurement of two indent lines with a target separation of  $5 \mu\text{m}$ . Positional information is extracted from the 3D measurement to produce a line profile plot of trough height and separation, Fig. 4(c). The AFM

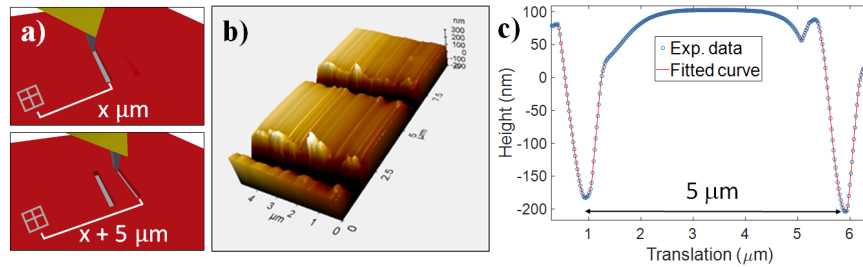


Fig. 4. (a) Diagram of probe tips physically producing controlled indent features into photo-resist layer relative to alignment marker; (b) 3-dimensional AFM topographic image of micro-tip indentations showing controlled separation distance; (c) Line profile of two relatively aligned indentations with a target controlled separation.

lateral resolution is  $\approx 30\text{nm}$  due to the AFM probe tip shape, but this can be reduced by curve fitting the measured data. By calculating the separation between the minimum point of each indentation, the average positional error over multiple tests is calculated as  $50\text{nm}$  with a standard deviation of  $\pm 50\text{nm}$ .

## 4. Micro assembly

### 4.1. Micro assembly of vertically coupled SOI ring resonators

The TP accuracies determined in the previous section allow the micro-assembly of vertically coupled Si ring resonators. A SEM image of a vertically coupled all-pass Si ring resonator assembled by our TP procedure is shown in Fig. 5(a). A high magnification SEM top-view image - Fig. 5(b) - shows the multi-layer waveguide coupling region with a targeted lateral alignment ( $\Delta x$ ) of  $400\text{nm}$  as defined in Fig. 2(a).

Conformation of the Si ultra-thin membrane promotes a strong bond between the SOI receiver substrate and the printed membrane, with the gradual conformation of the silicon membrane over the underlying waveguide shown in Fig. 5(c). The small aspect ratio of the waveguide height ( $320\text{nm}$ ) to the distance between contact points ( $\approx 5\mu\text{m}$ ) gives a radius of curvature of  $\approx 20\mu\text{m}$ , assuming a symmetrical s-bend deformation of the membrane. Due to the high confinement factor in the vertical direction of the ridge waveguide this means that the bend loss of the membranes is negligible compared to the losses from the ring resonator structure and will not significantly contribute to the overall loss of the membrane ring resonator devices.

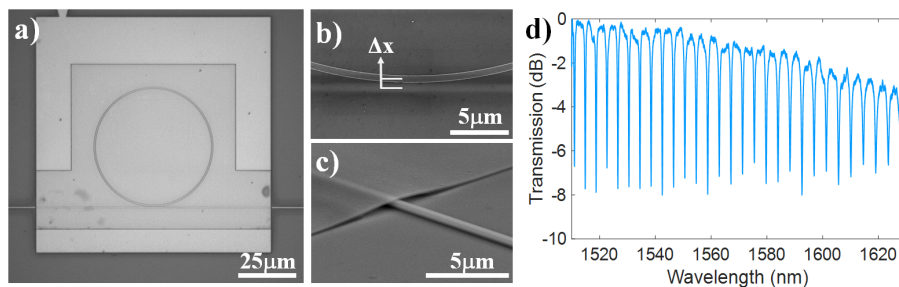


Fig. 5. (a) SEM image of membrane waveguide ring resonator bonded to a SOI bus waveguide; (b) SEM top-view image of interlayer waveguides with a controlled lateral alignment optimising the waveguide coupling; (c) SEM image of membrane conforming over waveguide structure with a membrane thickness of  $150\text{nm}$ ; (d) Measured transmission spectrum of the Si ring resonator vertically coupled to a SOI bus waveguide.

The transmission spectra of the micro assembled Si devices are measured using an end-fire rig set-up. TE polarised light is coupled from a tunable CW N-IR laser (Agilent 81640A, Keysight technologies) to the on-chip waveguides by a lensed fibre with an average injection power of  $350\mu\text{W}$ . Output light is captured using an InGaAs photo-detector and oscilloscope triggered by the tunable laser.

The transmission spectra for a fully assembled ring resonator device for the wavelength range of 1510-1630nm is presented in Fig. 5(d). It features single-mode repeated resonances with a FSR $\approx 4\text{nm}$  as expected from a  $25\mu\text{m}$  radius single-mode Si ring resonator.

The reduction in the quality of the Si membrane ring resonator devices as compared with similar monolithically realised devices can be attributed to increased scattering losses. This effect was due to the silica undercladding of the membrane devices not being fully removed during the HF vapour etch, leading to a thin, non-uniform silica surface on the membrane underside.

#### 4.2. Nanoscale placement accuracy

Positional accuracy of our TP procedure is measured by controlling the lateral alignment between the printed membrane waveguide and underlying bus waveguide. Varying the lateral position offset between the two results in a change in the coupling coefficient and the loaded quality factor of the final assembled Si ring resonator device.

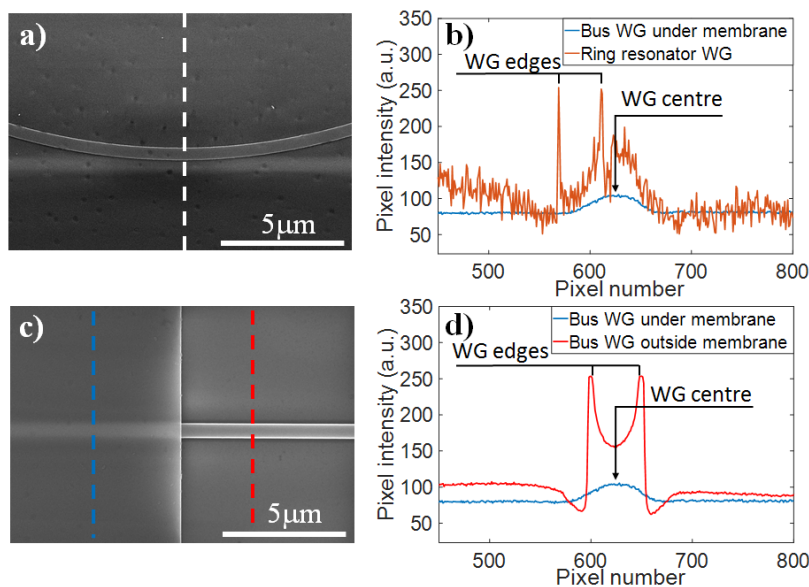


Fig. 6. (a) SEM image and (b) associated line sections of the coupler region of a micro-assembled ring resonator. The orange line profile corresponds to the dotted line in the image. The blue line profile is the averaged intensity taken from the bus waveguide sections at the left and right hand sides of the image; (c) SEM image and (d) line profiles of the bus waveguide as imaged through the membrane and in isolation.

The achieved waveguide lateral separation,  $\Delta x$ , is measured using a top view SEM image of the coupler region, showing both the membrane ridge waveguide and underlying bus waveguide, as illustrated in Fig. 6. The membrane ridge waveguide position is measured by taking a line profile of the SEM image, due to high scattering at the waveguide edges these features are easily resolvable. The waveguide centre position is taken as the average spatial position between the two edge points. The underlying bus waveguide position is taken as the centre of the slowly varying envelope of the electron scattering through the membrane, as shown in Fig. 6(b). To minimise



noise in the image, the bus waveguide envelope was calculated as the average of a number of line sections at either side of the coupling point. In order to ensure that the scattering through the membrane had a negligible effect on the measured central position, an image was taken at the point where the bus waveguide emerges from the membrane section. The centre point of the waveguide was calculated using the edge detection method in the exposed region and the envelope central position in the membrane covered region. Both methods produced a result within the pixel resolution of the image. Finally, by taking the difference between the measured positions of the membrane and bus waveguides, the offset,  $\Delta x$ , was calculated. The pixel resolution of the SEM images is in the range of  $\pm 10$  nm.

The controlled alignment of several micro-assembled ring resonators is demonstrated in Fig. 7 with their associated transmission spectra over a 20nm wavelength range centred at 1550nm. SEM images show the change in lateral alignment of the device coupler regions with targeted lateral offsets ( $\Delta x$ ) of 0nm, 300nm, 400nm and 500nm and a fixed vertical coupling gap of  $\approx 100$ nm, applied by the use of an intermediate HSQ spacer layer. The lateral offsets of the waveguides were assessed using the SEM method and produced an average positional alignment offset error of  $100 \pm 70$  nm, as detailed in Table 2.

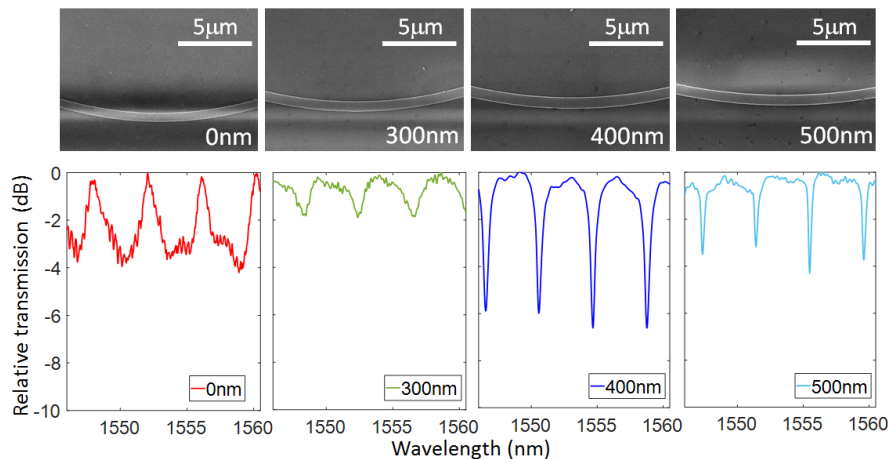


Fig. 7. SEM images showing the variation in positional waveguide alignments and targeted separation, including corresponding transmission spectra.

The measured transmission spectra clearly show the variation in optical coupling for the different devices. The resonance linewidth is reducing with increasing gap as expected, as a larger  $\Delta x$  will result in a reduced coupling coefficient between the ring and the bus waveguide. In the case of  $\Delta x = 0$ nm the transmission spectra does not represent a well defined ring resonator. Eigenmode expansion simulations of the optical mode show that for  $\Delta x = 0$ nm and a vertical separation between the waveguides of  $\approx 100$ nm, corresponding to the thickness of the HSQ spacer, the coupler region operates in a multimode regime producing complex coupling and loss behaviour as a function of wavelength. The transition to behaviour as an evanescent field coupler is reached for a lateral offset of greater than 200nm.

For the devices with  $\Delta x \geq 300$ nm, we extract the coupling coefficient and quality factor as shown in Table 2. These can be obtained by curve fitting each transmission spectrum to an analytic model of an all-pass ring resonator [30] in which coupling coefficient is a free parameter. In accordance with the reduction in linewidth, an increase in quality factor of the ring resonance as well as a reduction in the coupling coefficient is demonstrated. The first three devices exhibit a placement accuracy better than 150 nm, as detailed in Table 2. The reduction in alignment accuracy, with respect to the registration measurements detailed above, is most likely due to

relative motion between the stamp and the membrane device. This is more evident in the device with a targeted separation of 500 nm that exhibits an absolute placement accuracy of 210 nm.

Table 2. Comparison of micro-assembled SOI ring resonators with varying lateral offsets

Expected $\Delta x$ (nm)	Meas. $\Delta x$ (nm)	Coupling coeff.	Q factor
0	55	-	-
300	330	75%	2000
400	530	50%	2500
500	710	34%	4100
Average error $\pm$ Std dev	100 $\pm$ 70		

## 5. Conclusions

In summary, a correlation alignment scheme is demonstrated for the high precision integration of multiple fully fabricated photonic devices. Two complementary test procedures demonstrated average absolute registration accuracy of  $\pm 50$ nm. Using this method, the micro-assembly of single-mode, membrane Si photonic structures by direct bonding is demonstrated including the integration of vertically coupled SOI ring resonators with an average printing placement accuracy of  $100\text{nm} \pm 70\text{nm}$ .

## Funding

Engineering and Physical Sciences Research Council (EPSRC) through Parallel Heterogeneous Integration of III-V Devices on Silicon Photonic Chips (EP/P013570/1, EP/P013597/1), Cornerstone (EP/L021129/1), and PhD studentship support, and by EU Horizon 2020 Project ROAM (ID:645361).

## Acknowledgments

The authors acknowledge the staff of the James Watt Nanofabrication Centre at the University of Glasgow.